METRICA
METRology Institutional CAtalog

ISTITUTO NAZIONALE DI RICERCA METROLOGICA
Repository Istituzionale

Implementation of a graphene quantum Hall Kelvin bridge-on-a-chip for resistance calibrations

This is the author's accepted version of the contribution published as:

Original
Implementation of a graphene quantum Hall Kelvin bridge-on-a-chip for resistance calibrations / Marzano, Martina; Kruskopf, Mattias; Panna, Alireza R; Rigosi, Albert F; Patel, Dinesh K; Jin, Hanbyul; Cular, Stefan; Callegaro, Luca; Elmquist, Randolph E; Ortolano, Massimo. - In: METROLOGIA. - ISSN 0026-1394. - 57:1(2020), p. 015007. [10.1088/1681-7575/ab581e]

Availability:
This version is available at: 11696/61071 since: 2020-01-27T12:09:58Z

Publisher:
IOP

Published
DOI:10.1088/1681-7575/ab581e

Terms of use:

This article is made available under terms and conditions as specified in the corresponding bibliographic description in the repository

Publisher copyright
Institute of Physics Publishing Ltd (IOP)
IOP Publishing Ltd is not responsible for any errors or omissions in this version of the manuscript or any version derived from it. The Version of Record is available online at DOI indicated above

(Article begins on next page)

12 October 2024

Implementation of a graphene quantum Hall Kelvin bridge-on-a-chip for resistance calibrations

Martina Marzano[1,2], Mattias Kruskopf[3,4], Alireza R. Panna[4], Albert F. Rigosi[4], Dinesh K. Patel[5], Hanbyul Jin[3], Stefan Cular[4], Luca Callegaro[2], Randolph E. Elmquist[4], Massimo Ortolano[1,2]

[1] Politecnico di Torino
Corso Duca degli Abruzzi 24, 10129 Torino, Italy
[2]INRIM — Istituto Nazionale di Ricerca Metrologica
Strada delle Cacce, 91, 10135 Torino, Italy
[3]University of Maryland
College Park, MD 20742, USA
[4]NIST — National Institute of Standards and Technology
Gaithersburg, MD 20899, USA
[5]National Taiwan University
Taipei 10617, Taiwan.

E-mail: `m.marzano@inrim.it`

Abstract. The unique properties of the quantum Hall effect allow one to revisit traditional measurement circuits with a new flavour. In this paper we present the first realization of a quantum Hall Kelvin bridge for the calibration of standard resistors directly against the quantum Hall resistance. The bridge design is particularly simple and requires a minimal number of instruments. The implementation here proposed is based on the *bridge-on-a-chip*, an integrated circuit composed of three graphene quantum Hall elements and superconducting wiring. The accuracy achieved in the calibration of a 12 906 Ω standard resistor is of a few parts in 10^8, at present mainly limited by the prototype device and the interferences in the current implementation, with the potential to achieve few parts in 10^9, which is the level of the systematic uncertainty of the quantum Hall Kelvin bridge itself.

PACS numbers: 73.43.-f, 06.20.fb, 06.30.Ka

Submitted to: *Metrologia*

1. Introduction

Highest-accuracy (10^{-9} level) bridges are based on the cryogenic current comparator (CCC) [1]. A CCC bridge operates in a low-noise, low-magnetic field liquid helium cryogenic environment independent from the one where the QHE is realized. To date, no competitive operation of a CCC in a cryogen-free environment has been demonstrated. Dedicated room-temperature DC current comparator (DCC) bridges can also be employed, though with limitations on the available resistance ratios (for instance, only the $R_\mathrm{H} : 1\,\mathrm{k}\Omega$ ratio might be available for the measurement of R_H), ratio errors at the 10^{-8} level, and low current in the QHE device [2]. Both CCC and DCC bridges are expensive instruments.

In [3] we introduced the design of a direct current (DC) quantum Hall Kelvin bridge for the direct calibration of standard resistors. Here we present a *bridge-on-a-chip* implementation: the core is an integrated circuit composed of three quantum Hall effect (QHE) elements fabricated using epitaxial graphene on a SiC substrate and interconnected by a NbTiN superconducting wiring layer [4, 5]. Each QHE element of the chip constitutes an arm of a Kelvin bridge; the fourth arm is given by the resistor under calibration. The bridge network is completed with inexpensive commercial room-temperature electronic instrumentation: a current generator and a digital voltmeter.

The conditions of temperature and magnetic field necessary to achieve quantization in graphene are less demanding than those of conventional GaAs devices [6–8]. The operation of graphene QHE devices in small-size dry cryostats was demonstrated [9, 10]. Therefore, the herewith presented bridge-on-a-chip has the potential to become a tabletop, continuously-operating QHR calibration system that does not require further high-accuracy commercial instrumentation.

The design of the bridge-on-a-chip stems from a schematic diagram proposed by Delahaye [11, figure 7], and later implemented in [12, 13], to test the reproducibility of the quantized Hall resistance (QHR). The operation of the bridge exploits the peculiarities of the QHE effect as a circuit element [14]: *multiple connections* [11] minimize the effect of cable resistances, and mimic the behaviour of the combining network of a conventional Kelvin bridge [15, section 4.6.3.4].

National metrology institutes (NMI) exploit the QHE as a realization of the unit of resistance [16, appendix 2]. The typical NMI traceability chain involves an experiment with a single QHE element in which a resistance bridge compares the quantized resistance $R_\mathrm{H} \approx 12\,906.4\,\Omega$ with the resistance of the artifact standard under calibration. The resistance standards of interest have nominal values in decadal sequence ($100\,\Omega$, $1\,\mathrm{k}\Omega$, ...) or equal to R_H [17, 18].

Section 2 presents the theory of operation of the bridge. Section 3 describes the device and its characterization. Section 4 describes the implemenetation of the experiment in the laboratories of the National Institute of Standards and Technology (NIST), Gaithersburg, MD, US. Sections 5 and 6 develop a detailed circuit model of the whole electrical network to evaluate the measurement uncertainty. The results reported in section 7 show that the bridge can calibrate a resistor having nominal value R_H with a relative uncertainty of a few parts in 10^9, thus comparable with that of the CCC bridge [2] employed during the validation measurements. As finally discussed in section 8, the bridge-on-a-chip concept can be extended to include quantum Hall array resistance standards [19, 20] in place of individual elements, thus allowing the calibration of resistance standards having nominal values different from R_H, like decadal ones.

2. Theory of operation

Figure 1 shows the principle schematic of the bridge. The ratio arm is composed of the two QHE elements U_2 and U_3; the opposite arm is composed of the QHE element U_1 and of the four-terminal resistor under calibration $R_x = R_\mathrm{H}(1 + x)$, x being the relative deviation of R_x from R_H. The bridge excitation current is I. The bridge operates in the *deflection mode*, that is, the measurand x is related to the bridge imbalance voltage V_D.

The QHE elements are joined by multiple connections [11]: U_1, U_2 and U_3 are connected by triple-series and -parallel connections; U_1 and U_3 are connected to R_x by a double-series connection between the current terminals and a single connection between the voltage terminals.

In figure 1, we considered, as an example, that all blue elements are implemented in a single device

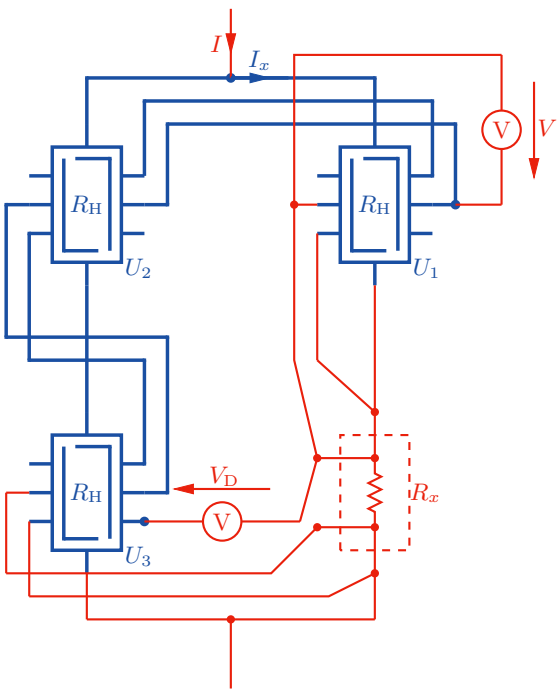

Figure 1. Principle schematic of the Kelvin bridge, adapted from figure 1 of [3] to match the implementation presented in section 4. The QHE elements U_1, U_2 and U_3 are interconnected by triple-series and -parallel connections. The four-terminal resistor under calibration R_x is connected to U_1 and U_3 by a double series connection between the current terminals and a single connection between the voltage terminals. I is the bridge excitation current and I_x is the current fraction crossing U_1 and R_x. $V = R_H I_x$ is the voltage drop across U_1 and V_D is the bridge imbalance differential voltage. Thick blue elements represent the device; thin red elements and connections are external to the device.

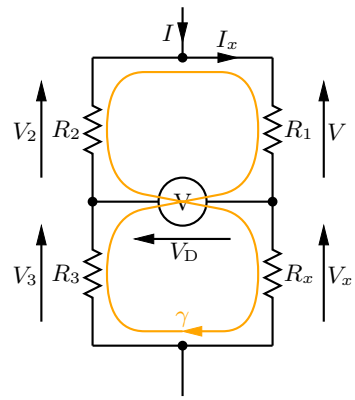

Figure 2. Bridge equivalent circuit in the ideal case. R_1, R_2 and R_3 are the resistances of the QHE elements U_1, U_2 and U_3, respectively. V, V_2 and V_3 correspond to the Hall voltages across U_1, U_2 and U_3. V_x is the voltage across the resistor under calibration R_x. The orange-highlighted 8-shaped path γ is a suitable path for the derivation of the bridge model.

and interconnected therein. The red colour, instead, identifies the four-terminal resistor under calibration and its connections to the QHE elements. The current I splits between the two bridge arms and I_x is the current crossing U_1 and R_x, such that $V = R_H I_x$ is the Hall voltage measured across U_1.

Figure 2 shows the bridge equivalent circuit in the ideal case, with zero lead and contact resistances, and infinite leakage resistances. Applying the Kirchhoff's voltage law to the 8-shaped path γ yields

$$-V_3 + V_D - V + V_2 + V_D + V_x = 0. \quad (1)$$

Taking into account that $V_x = (R_x/R_1)V$ and that for ideal QHE elements $R_1 = R_2 = R_3$ and $V_2 = V_3$, we obtain the measurement model in the ideal case:

$$x = -2\frac{V_D}{V}. \quad (2)$$

3. Bridge-on-a-chip description and characterization

In general, the bridge-on-a-chip can be implemented with any type of QHE elements (e.g., GaAs or graphene) and with conventional double- or triple-connections, according to the schematic of figure 1.

Here, the bridge was implemented using a prototype quantum Hall array resistance standard (QHARS) composed of three multiple-series and parallel interconnected graphene Hall bars. To reduce the effect of contact resistances, split contacts are applied as described in [4]. Furthermore, the array elements use superconducting interconnections that do not have ohmic resistance and do not suffer from magnetoresistance. This allows the potential contacts to be directly connected to the current path, making the QHARS as precise and stable as single-element quantized Hall resistance standards [5]. Exploiting the superconducting interconnections, this kind of device differs from a conventional one for being crossover free. Both the split contacts and the interconnections are made of NbTiN.

Figure 3 shows the mounted sample and the design details of the array device. In figures 3(b) and (c), the sample characterization by confocal laser scanning microscopy [21] shows the NbTiN interconnections and

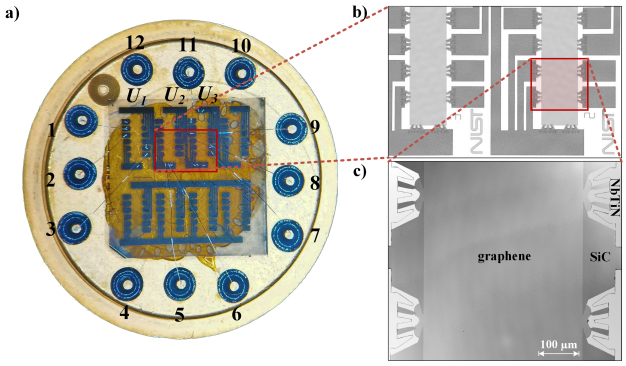

Figure 3. (a) The sample was mounted and contacted using a TO-8 header such that only three in series connected devices were active for the measurements. (b) The modified optical microscope image shows design details of the crossover-free multiple connection in the highlighted region of (a). By using superconducting NbTiN, ohmic resistances and magnetoresistance contributions in the interconnections are avoided. (c) The confocal laser scanning microscope image indicated in (b) shows the split contact geometry as a part of the multiple connection that rejects the influence of contact resistances.

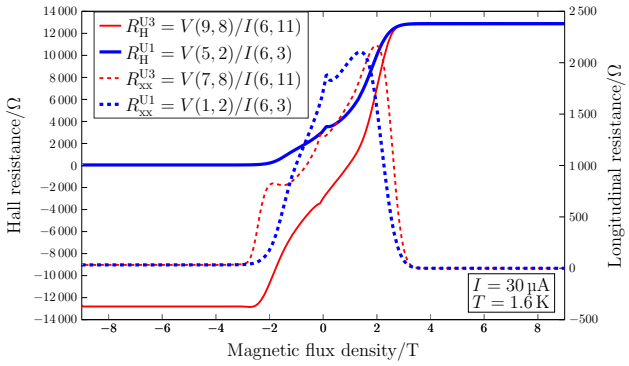

Figure 4. Preliminary characterization of the array device at 30 µA and 1.6 K. The plot shows the magnetic field dependence of the Hall resistance R_H (solid lines, left axis) and longitudinal resistance R_{xx} (dashed lines, right axis) of U_1 (thick blue) and U_3 (thin red). In the legend, $V(i,j)$ represents the voltage measured across the terminals i and j of figure 3, while $I(l,m)$ represents the current entering into terminal l and exiting from terminal m.

split contacts as well as the structured monolayer graphene Hall bar.

The graphene growth process that applies a combination of face-to-graphite (FTG) and polymer-assisted sublimation growth (PASG), and the device fabrications process are thoroughly described in previous works [4, 7, 22, 23]. For charge carrier density control, the graphene was functionalized with $Cr(CO)_3$ after device fabrication in a purpose-built deposition chamber [24].

Figure 4 shows a preliminary characterization of the array device at about 1.6 K performed with a lock-in amplifier system. The individual magnetic

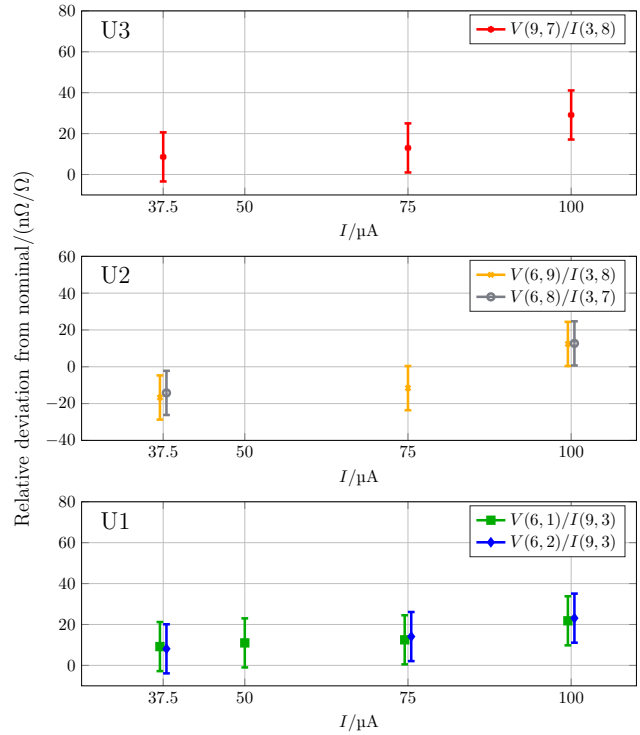

Figure 5. Relative deviation of the Hall resistance R_H from the nominal value of U_1, U_2 and U_3 at 9 T, 1.6 K and different nominal current values I_x (37.5 µA, 50 µA, 75 µA and 100 µA). For the elements U_1 and U_2 there are reported the measurements performed with two different terminal configurations. At overlapping points a small horizontal offset has been introduced to improve readability. The plot shows the expanded uncertainties ($k = 2$).

field dependence of the Hall resistance R_H and of the longitudinal resistance R_{xx} of U_1 and U_3 were measured in the four-terminal resistance measurement configuration with a current of about 30 µA for each QHE element. In the legend of figure 4, $V(i,j)$ represents the voltage measured across the terminals i and j of figure 3, while $I(l,m)$ represents the current entering into terminal l and exiting from terminal m.

The measurements of R_H and R_{xx} for both of these devices (U_1 and U_3) are asymmetric with respect to the magnetic field direction, with a plateau starting around $B = \pm 3$ T. When the magnetic field direction is positive, both the elements exhibit the typical behaviour of R_H and R_{xx}. Instead, when the magnetic field is reversed, the behaviour of R_{xx} and R_H is atypical for both elements due to the different current paths caused by the position of the measurement terminals and the multiple-connections between the devices [4].

Figure 5 shows, at 9 T and 1.6 K, the relative deviation of the Hall resistance R_H from the nominal value of U_1, U_2 and U_3 for different values of the current I_x injected in each QHE element. The traceability of

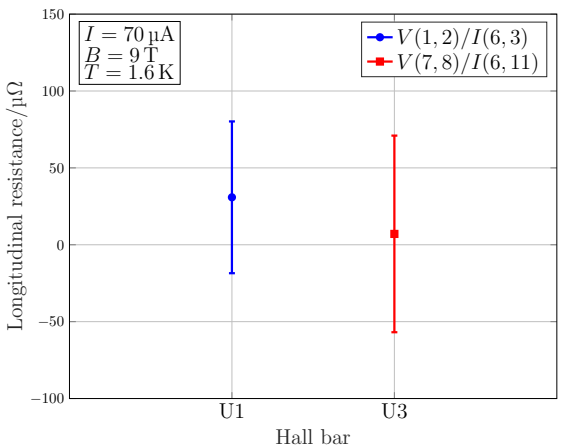

Figure 6. Longitudinal resistances R_{xx} measurements of U_1 and U_3 at 70 µA, 1.6 K and 9 T.

the measurement is obtained by comparing the Hall resistances with a room-temperature 100 Ω resistance standard (Electro Scientific Industries ESI SR102‡) calibrated against a GaAs QHR with a binary cryogenic current comparator (BCCC) bridge [25]. The plot reports also the expanded uncertainties with coverage factor $k = 2$. The deviation increases with the current because of the self-heating. For currents up to 75 µA, that is, within the range usually employed in the calibrations, the quantized Hall resistance has a deviation less than $20\,\mathrm{n\Omega\,\Omega^{-1}}$. For U_1 and U_2 there are reported the measurements performed with two different terminal configurations.

Figure 6 shows more accurate measurements at 70 µA, 1.6 K and 9 T of the longitudinal resistance R_{xx} of U_1 and U_3 by using an analog nanovoltmeter and a current reversal measurement technique to eliminate offsets. The resistances are zero within the measurement uncertainty, $R_{xx}^{U1} = (31 \pm 49)\,\mu\Omega$ and $R_{xx}^{U3} = (7 \pm 64)\,\mu\Omega$. Here the uncertainty bars represent the standard uncertainty.

4. Experimental setup

The bridge operates in a cryogenic system at about 1.5 K and at a magnetic flux density of 9 T.

Figure 7 shows the implementation of the bridge: the blue elements and connections represent the device as described in section 3; the red element and connections represent the four-terminal resistor under calibration and its connections with the device and current source; and the green elements represent the voltmeter used to measure the bridge voltages.

‡ Commercial equipment, instruments, and materials are identified in this paper in order to specify the experimental procedure adequately. Such identification is not intended to imply recommendation or endorsement by the National Institute of Standards and Technology or the United States government, nor is it intended to imply that the materials or equipment identified are necessarily the best available for the purpose.

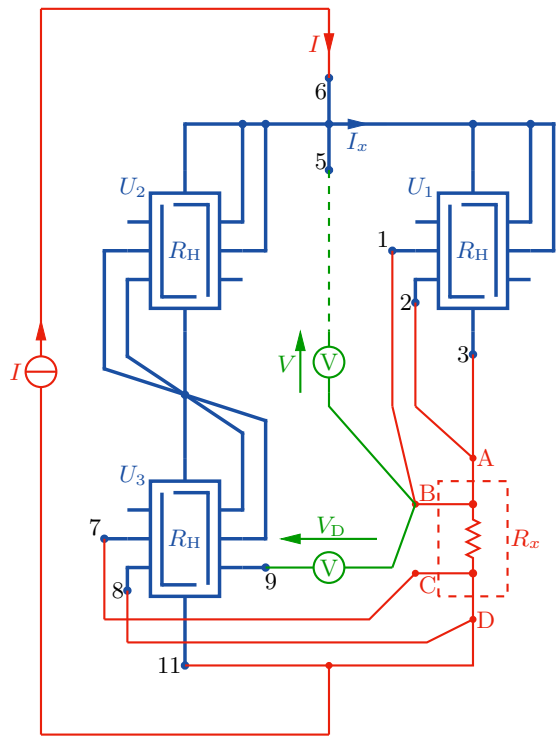

Figure 7. Schematic of the bridge implementation representing the crossover-free multiple connections.

The connections are labelled with numbers corresponding to the wire-bonded TO-8 holder pins, shown in figure 3.

The four-terminal resistor under calibration is a 12.9 kΩ NIST resistance standard (NIST ESI SP036), kept in a temperature-controlled oil bath at 25 °C. The standard resistor is located in a different laboratory and connected to the bridge through long shielded cables at junction terminals A, B, C and D. The distance between the junction terminals and R_x is of about 10 m.

The bridge excitation current I is generated by an Adret 103A direct current and voltage standard. The voltages V and V_D are alternatively measured with an Agilent 34420A nanovoltmeter manually switched between the two positions.

The measured data are acquired with an application developed under the National Instruments Labview environment.

5. Error sources

We list and analyze here the error sources affecting the bridge measurement, and for each error source we construct a suitable mathematical model. The

individual error terms are collected in section 6 into a complete measurement model, which is then used in section 7 to evaluate the uncertainty.

We discuss first the errors due to the bridge network and instrumentation, that is, bias and drift, voltmeter error, lead, contact and leakage resistances. These errors depend on the practical implementation of the bridge and exist also with ideal QHE elements. We discuss last the error caused by the possible imperfect quantization of the QHE devices. This error mainly depends on the device fabrication and the operating conditions.

The effects of lead, contact and leakage resistances are analyzed with the computer method presented in [26, 27] which directly yields the analytical expression of the errors.

5.1. Bias and drift

The readings of the bridge voltages may be biased due to the thermoelectric voltages in the bridge circuit and to the voltmeter residual offset and bias current. This bias may also drift with time. Bias and drift can be removed by periodically reversing the bridge excitation with a suitable pattern [28, 29].

In this work, the excitation current I is periodically reversed with the sign pattern $-++-$, yielding associated raw readings $V_{\mathrm{D}}^{\mathrm{read},1}$ $(-)$, $V_{\mathrm{D}}^{\mathrm{read},2}$ $(+)$, $V_{\mathrm{D}}^{\mathrm{read},3}$ $(+)$ and $V_{\mathrm{D}}^{\mathrm{read},4}$ $(-)$. The reading $V_{\mathrm{D}}^{\mathrm{read}}$ of the imbalance voltage is obtained by combining the raw readings as

$$V_{\mathrm{D}}^{\mathrm{read}} = \frac{1}{4}(-V_{\mathrm{D}}^{\mathrm{read},1} + V_{\mathrm{D}}^{\mathrm{read},2} + V_{\mathrm{D}}^{\mathrm{read},3} - V_{\mathrm{D}}^{\mathrm{read},4}). \quad (3)$$

Similarly, for the Hall voltage,

$$V^{\mathrm{read}} = \frac{1}{4}(-V^{\mathrm{read},1} + V^{\mathrm{read},2} + V^{\mathrm{read},3} - V^{\mathrm{read},4}). \quad (4)$$

The above pattern removes bias and first-order drift [28, 29].

It is worth noting that if there is an asymmetry between positive and negative excitation, this can be assimilated to a bias with respect to the mean excitation and thus removed by (3) and (4), provided indeed that the mean excitation is sufficiently stable between the measurement phase of V_{D} and that of V.

5.2. Voltmeter error

Let V_{D} be the bridge imbalance voltage for positive excitation and $-V_{\mathrm{D}}$ that for negative excitation. For the measurement of V_{D}, we assume that the voltmeter systematic error can be decomposed into a gain error g_{D}, an offset error $V_{\mathrm{D,OS}}$ and a nonlinearity error $\Delta V_{\mathrm{D}}^{\pm}$

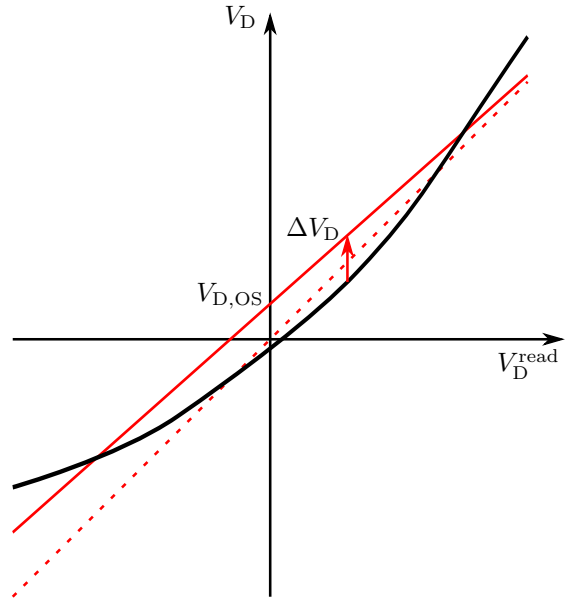

Figure 8. Voltmeter transfer characteristic relating the imbalance voltage V_{D} to the voltmeter reading $V_{\mathrm{D}}^{\mathrm{read}}$: the solid black curve represents the voltmeter transfer characteristic; the solid red line represents a linear approximation with slope $1 + g_{\mathrm{D}}$ and offset $\Delta V_{\mathrm{D,OS}}$; and the dashed red line with unit slope represents the ideal transfer characteristic. The vertical deviation between the linear approximation and the transfer characteristic is the nonlinearity error ΔV_{D}.

(figure 8), so that for the readings in the pattern $-++-$ we can write

$$\begin{aligned} -V_{\mathrm{D}} &= (1+g_{\mathrm{D}})V_{\mathrm{D}}^{\mathrm{read},1} + V_{\mathrm{D,OS}} - \Delta V_{\mathrm{D}}^{-}, \\ V_{\mathrm{D}} &= (1+g_{\mathrm{D}})V_{\mathrm{D}}^{\mathrm{read},2} + V_{\mathrm{D,OS}} - \Delta V_{\mathrm{D}}^{+}, \\ V_{\mathrm{D}} &= (1+g_{\mathrm{D}})V_{\mathrm{D}}^{\mathrm{read},3} + V_{\mathrm{D,OS}} - \Delta V_{\mathrm{D}}^{+}, \\ -V_{\mathrm{D}} &= (1+g_{\mathrm{D}})V_{\mathrm{D}}^{\mathrm{read},4} + V_{\mathrm{D,OS}} - \Delta V_{\mathrm{D}}^{-}. \end{aligned} \quad (5)$$

Combining the above equations as in (3) yields

$$V_{\mathrm{D}} = (1+g_{\mathrm{D}})V_{\mathrm{D}}^{\mathrm{read}} - \Delta V_{\mathrm{D}}, \quad (6)$$

with $\Delta V_{\mathrm{D}} = (\Delta V_{\mathrm{D}}^{+} - \Delta V_{\mathrm{D}}^{-})/2$. The terms g_{D} and ΔV_{D} can be assumed to have zero value with uncertainties that can be evaluated from the voltmeter specifications.

Similarly, for the Hall voltage, we can write

$$V = (1+g)V^{\mathrm{read}} - \Delta V. \quad (7)$$

Generally, the voltmeter is used for the measurement of ΔV_{D} and V in two different ranges, and the quantities g_{D}, g, ΔV_{D} and ΔV can be thus considered uncorrelated.

5.3. Lead and contact resistances

Figure 9 shows an equivalent circuit representing the most significant lead and contact resistances of the implemented bridge. Lead resistances from the bridge-on-a-chip to the junction terminals A, B, C and D

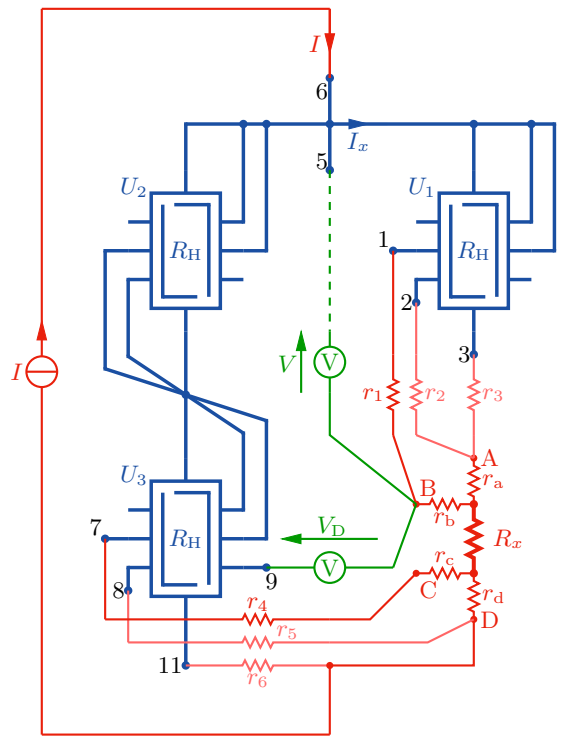

Figure 9. Bridge equivalent circuit representing the most significant lead and contact resistances (contact resistances are incorporated into lead resistances). Letter subscripts identify the lead resistances associated to the four-terminal resistor under calibration; number subscripts identify the resistances associated to the connections to the cryogenic system.

are labelled from r_1 to r_6; lead resistances from the junction terminals to R_x are labelled from r_a to r_d.

Assuming lead resistances much less than R_H, the analysis of this circuit according to [26, 27] yields the relationship

$$x = -2\frac{V_D}{V} - \Delta x^{\text{leads}} \tag{8}$$

with

$$\Delta x^{\text{leads}} = \frac{1}{R_H^2}\left[r_a(r_b - r_1) + (r_c + r_4)r_d\right] + O\left(\frac{r_{\max}}{R_H}\right)^3, \tag{9}$$

where $r_{\max}$ is the maximum lead resistance of a connection and the *big O notation* specifies the limit on the growth rate of the higher-order terms.

The error term Δx^{leads} depends at second order on the lead resistances r_1, r_a, r_b, $r_c + r_4$, and r_d. Instead, the resistances r_2, r_3, r_5 and r_6 contribute only at third order, as expected from a triple-series connection [11].

Conventional Kelvin bridges include, in addition to the main voltage ratio arm—R_2 and R_3 of figure 2—the *Kelvin arm*, a network of two additional resistors combining [30] the potentials at the low-voltage terminals (not shown in figure 2) of R_1 and R_x. Looking at figure 9, terminal 1 of U_1 takes a role analogous to the low-voltage terminal of R_1; r_b and r_1 constitute a Kelvin arm for the voltage drop on r_a. The term $r_a(r_b - r_1)$ in (9) models the contribution to Δx^{leads} caused by the imbalance of this Kelvin arm. It is worth mentioning that, with respect to a conventional Kelvin bridge, the imbalance of the Kelvin arm has a second order effect on Δx^{leads} due to the properties of the QHE, which scale down the current in the Kelvin arm.

5.4. Leakage resistances

Figure 10 shows the bridge equivalent circuit with the leakage resistances of interest: R_{CL} represents the resistance from the voltmeter low terminal to ground, including the interconnection leakage resistances and the voltmeter common-mode resistance; likewise, R_{CH} represents the resistance from the high terminal to ground; and R_D represents the voltmeter differential resistance. The voltages V_{DL} and V_{DH} are, respectively, the voltage of the low and high voltmeter terminals with respect to ground, so that $V_D = V_{DH} - V_{DL}$.

The effect of leakage resistances is usually nulled by keeping $V_{DL} \approx V_{DH} \approx 0$ either by directly grounding V_{DL} or by means of a Wagner ground. This was not possible in the experiment described here due to ground interferences between the laboratory hosting the bridge and that hosting the standard resistor. We therefore adopted a different approach: the ground is switched between the low (IL in figure 10) and the high (IH in figure 10) terminals of the current source and the voltmeter readings are averaged, thus cancelling the effect of leakage resistances at first order.

Let V_D and V be now, respectively, the average imbalance and Hall voltages. The analysis of the circuit of figure 10 yields the relationship

$$x = -2\frac{V_D}{V} - \Delta x^{\text{leak}} \tag{10}$$

with

$$\Delta x^{\text{leak}} = 2\frac{V_D}{V}\left(\frac{R_H}{2R_{CL}} + \frac{3R_H}{2R_D}\right) - \frac{R_H}{R_{CL}}\left(\frac{R_H}{R_{CH}} - \frac{R_H}{2R_{CL}}\right). \tag{11}$$

Leakage resistances thus cause both multiplicative and additive errors.

5.5. Imperfect quantization

With reference to figure 2, we here consider the possible imperfect quantization of the QHE elements by setting $R_1 = R_H(1 + x_1)$, $R_2 = R_H(1 + x_2)$ and $R_3 = R_H(1 + x_3)$. The relative deviations x_1, x_2 and x_3 of the resistances from R_H represent the quantization

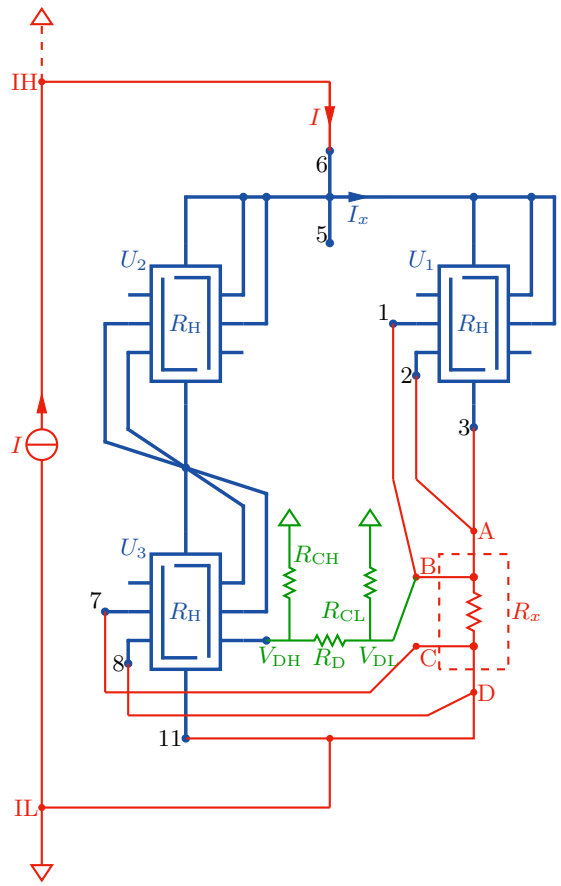

Figure 10. Bridge equivalent circuit representing the leakage resistances of interest. IL and IH represent the low and high terminals of the current source, which are alternatively connected to ground to reduce the effect of leakage resistances.

errors. The voltages V, V_2, V_3 and V_x of (1) can be written as

$$\begin{aligned} V &= R_\mathrm{H}(1+x_1)I_x, \\ V_2 &= R_\mathrm{H}(1+x_2)(I-I_x), \\ V_3 &= R_\mathrm{H}(1+x_3)(I-I_x), \\ V_x &= R_\mathrm{H}(1+x)I_x. \end{aligned} \tag{12}$$

By substituting the above expressions into (1) and simplifying, we obtain

$$R_\mathrm{H}(I-I_x)(x_2-x_3) + R_\mathrm{H}I_x(x-x_1) + 2V_\mathrm{D} = 0. \tag{13}$$

Since all terms in (13) are at first order in x, x_1, x_2 and x_3, the currents I_x and $(I-I_x)$ can be approximated at the zeroth order, that is,

$$R_\mathrm{H}(I-I_x) \approx R_\mathrm{H}I_x \approx V. \tag{14}$$

Therefore, with this assumption, we obtain the relationship

$$x = -2\frac{V_\mathrm{D}}{V} - \Delta x^\mathrm{quant} \tag{15}$$

with

$$\Delta x^\mathrm{quant} = -x_1 + x_2 - x_3. \tag{16}$$

6. Measurement procedure and model

According to the discussion of the previous section, in particular for the minimization of the effect of leakage resistances, we adopt the following measurement procedure for a single measurement (all readings are obtained by periodically reversing the excitation current I according to the pattern $-++-$):

(i) Ground the current source low terminal.

(ii) Record repeated readings of V_D and compute their average $V_\mathrm{D}^\mathrm{read,low}$.

(iii) Record repeated readings of V and compute their average $V^\mathrm{read,low}$.

(iv) Ground the current source high terminal.

(v) Record repeated readings of V_D and compute their average $V_\mathrm{D}^\mathrm{read,high}$.

(vi) Record repeated readings of V and compute their average $V^\mathrm{read,high}$.

(vii) Compute the averages $V_\mathrm{D}^\mathrm{read} = (V_\mathrm{D}^\mathrm{read,low} + V_\mathrm{D}^\mathrm{read,high})/2$, $V^\mathrm{read} = (V^\mathrm{read,low} + V^\mathrm{read,high})/2$ and the bridge reading $x^\mathrm{read} = -2V_\mathrm{D}^\mathrm{read}/V^\mathrm{read}$.

The above steps are then repeated for multiple measurements.

Given the above procedure, we can combine the results reported in section 5 to obtain the complete measurement model,

$$x = -2\frac{V_\mathrm{D}}{V} - \Delta x^\mathrm{leads} - \Delta x^\mathrm{leak} - \Delta x^\mathrm{quant}, \tag{17}$$

$$= -2\frac{(1+g_\mathrm{D})V_\mathrm{D}^\mathrm{read} - \Delta V_\mathrm{D}}{(1+g)V^\mathrm{read} - \Delta V} - \Delta x^\mathrm{leads} - \Delta x^\mathrm{leak} - \Delta x^\mathrm{quant}, \tag{18}$$

where we have assumed that the nonlinearity errors ΔV_D and ΔV are the same for the grounded-low and grounded-high readings. Taking into account that g_D, g, $\Delta V_\mathrm{D}/V^\mathrm{read}$ and $\Delta V/V^\mathrm{read}$ are all small quantities with respect to one, the above model simplifies as

$$x = \left(1 + g_\mathrm{D} - g + \frac{\Delta V}{V^\mathrm{read}}\right)x^\mathrm{read} - 2\frac{\Delta V_\mathrm{D}}{V^\mathrm{read}} - \Delta x^\mathrm{leads} - \Delta x^\mathrm{leak} - \Delta x^\mathrm{quant}. \tag{19}$$

7. Results

The quantum Hall Kelvin bridge was validated with the comparison procedure schematically represented in figure 11. First, the quantum Hall Kelvin bridge was used to calibrate the NIST SP036 resistance standard directly against the graphene QHR, obtaining x from (19). Then, the same NIST SP036 resistance standard was calibrated with a commercially available CCC [25] against a 100 Ω resistance standard (ESI SR102), in turn calibrated with the CCC against a

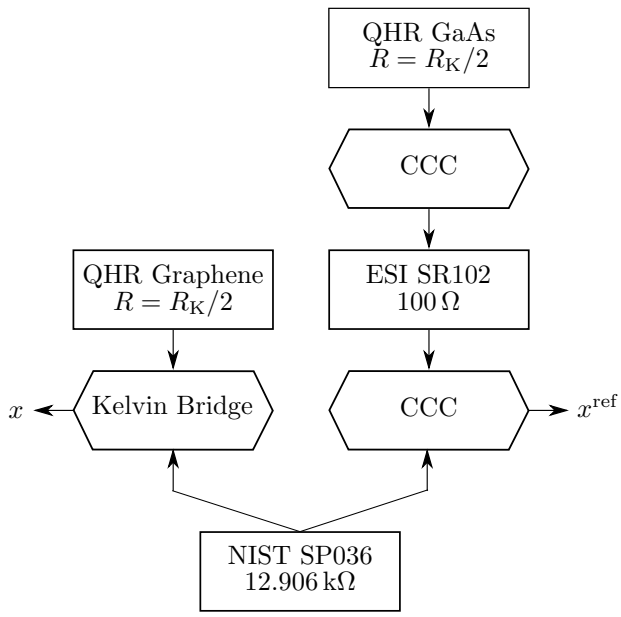

Figure 11. Diagram representing the comparison between the calibration of the NIST SP036 resistance standard performed with the Kelvin bridge and that performed with the CCC.

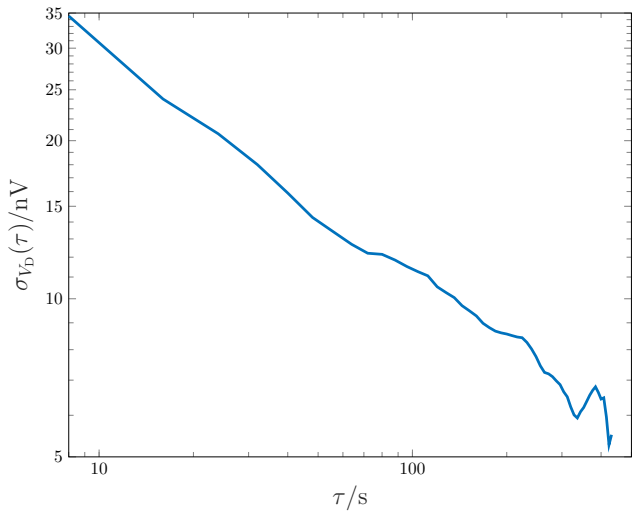

Figure 12. Allan deviation $\sigma_{V_D}(\tau)$ of the bridge imbalance voltage as a function of the integration time τ for an example measurement.

GaAs QHR. This yielded x^{ref}, the reference relative deviation of R_x from R_H. The result of the comparison is the difference δ between the calibration with the quantum Hall Kelvin bridge and that with the CCC, that is,

$$\delta = x - x^{ref} \tag{20}$$

$$= \left(1 + g_D - g + \frac{\Delta V}{V^{read}}\right) x^{read} - 2\frac{\Delta V_D}{V^{read}} - \Delta x^{leads} - \Delta x^{leak} - \Delta x^{quant} - x^{ref} \tag{21}$$

$$= \left(1 + g_D - g + \frac{\Delta V}{V^{read}}\right) x^{read} - 2\frac{\Delta V_D}{V^{read}} - \Delta x^{leads} - \Delta x^{leak} + x_1 - x_2 + x_3 - x^{ref}. \tag{22}$$

The uncertainty budget for δ of an example comparison is reported in table 1. The comparison was performed with $I \approx 150\,\mu A$ so that the current in the QHE elements is $I_x \approx I/2 \approx 75\,\mu A$.

The first uncertainty component is the type A uncertainty of the bridge reading x^{read}. The reported measurement consisted of 4 repeated cycles, as described in section 6. Taking into account the dead time between the readings, the overall measurement time was about 3 h. Figure 12 reports an example Allan deviation of the imbalance voltage V_D, as a function of the effective integration time τ. The slope of about $-1/2$ of the Allan deviation in the log-log plot means that the dominant noise process is white [31]. The type A uncertainty was evaluated accordingly. It should be noted that the ultimate limit due to the thermal and voltmeter noise is about one order of magnitude below the level shown in figure 12. This observed level is probably due to fluctuations in the thermal voltages along the circuit and external interferences, both fed by the presented implementation spanning two laboratories.

The components from 2 to 5 are the type B uncertainties of the nanovoltmeter measuring V_D and V, considering both gain and nonlinearity as described in section 5. The measurement ranges for V_D and V were 1 mV and 1 V, respectively (V_D is of the order of a few microvolts; V is about 0.5 V or 1 V, depending on the current). The uncertainty components were evaluated from the instrument specifications, assuming uniform probability distributions for the errors. The uncertainty components associated with V are virtually negligible.

Component 6 is the correction for the lead resistances estimated from (9), considering the resistance measurements $r_1 \approx 1.43\,\Omega$, $r_4 \approx 2.30\,\Omega$, $r_a \approx 0.888\,\Omega$, $r_b \approx 0.888\,\Omega$, $r_c \approx 0.892\,\Omega$ and $r_d \approx 0.894\,\Omega$ with a relative uncertainty of 1 %. The values of r_1 and r_4 mainly depend on the cabling of the cryogenic probe which is made of wires with small cross section to reduce the heat exchange with the environment. These values are typical of QHE cryogenic systems and cannot be easily reduced. The values of r_a, r_b, r_c and r_d are large because the NIST SP036 resistance standard was located in a different laboratory. These resistance values yield an error $\Delta x^{leads} = 1.42 \times 10^{-8}$ that needs to be corrected. Alternatively, this error can be reduced by either implementing the experiment in a more compact way or by connecting nodes 2, 3, 8 and 11 directly to the current terminals of the resistance standard to reduce

Table 1. Uncertainty budget for δ of an example comparison performed with $I \approx 150\,\mu\text{A}$. Each input quantity is identified by the index i, its name and the symbol x_i. $c_i = \partial\delta/\partial x_i$ is the sensitivity coefficient of δ with respect to x_i. RSS denotes the root sum of squares.

i	Quantity name	Quantity	x_i	$u(x_i)$	Type	c_i	$u_i(x) = \lvert c_i \rvert u(x_i)$
1	Bridge reading ($\approx 3\,\text{h}$)	x^{read}	-3.4567×10^{-6}	5.5×10^{-9}	A	1.0	5.5×10^{-9}
2	Nanovoltmeter gain (V_{D})	g_{D}	0	2.9×10^{-5}	B	-3.5×10^{-6}	0.1×10^{-9}
3	Nanovoltmeter gain (V)	g	0	2.0×10^{-5}	B	3.5×10^{-6}	$< 0.1 \times 10^{-9}$
4	Nanovoltmeter nonlinearity (V_{D})	ΔV_{D}	0	$0.3\,\text{nV}$	B	$-2.1\,\text{V}^{-1}$	0.6×10^{-9}
5	Nanovoltmeter nonlinearity (V)	ΔV	0	$740\,\text{nV}$	B	$-3.6 \times 10^{-6}\,\text{V}^{-1}$	$< 0.1 \times 10^{-9}$
6	Lead resistances	Δx^{leads}	1.42×10^{-8}	0.2×10^{-9}	B	-1	0.2×10^{-9}
7	Leakage resistances	Δx^{leak}	$< 10^{-11}$	$< 10^{-11}$	B	-1	$< 0.1 \times 10^{-9}$
8	Imperfect quantization	Δx^{quant}	-3.71×10^{-8}	0.7×10^{-9}	B	-1	0.7×10^{-9}
9	CCC calibration	x^{ref}	-3.4366×10^{-6}	0.4×10^{-9}	B	-1	0.4×10^{-9}
		δ	2.7×10^{-9}		RSS		5.6×10^{-9}

r_{a} and r_{d}.

Component 7 is the correction for the leakage resistances estimated from (11), considering leakage resistance measurements on the bridge network and the instrument specifications. With R_{CL}, R_{CH} and R_{D} greater than $10\,\text{G}\Omega$, this uncertainty component is negligible.

Component 8 is the correction for the imperfect quantization of the device, as characterized in section 3. The error $\Delta x^{\text{quant}} = -3.71 \times 10^{-8}$, which combines the quantization errors of all three QHE elements according to 16, is related to the specific prototype device and to the current dependence of the bridge quantized Hall resistances: a recent work has shown that such devices can reach an accuracy level of 10^{-9} [5].

Component 9 is the reference deviation of R_x from R_{H} of the NIST SP036 resistance standard obtained from the CCC calibration. This uncertainty component considers also the instability of the resistance standards between the Kelvin bridge and the CCC calibrations.

Components 8 and 9 are set apart in the uncertainty budget because they were both determined from CCC measurements against the same ESI SR102 $100\,\Omega$ resistance standard and are therefore partially correlated. The correlated part, by virtue of (16), actually cancels in (22) and the remaining uncertainty components are those associated to the type A uncertainty.

The result of the example comparison is the difference, from (21), $\delta = (2.7 \pm 5.6) \times 10^{-9}$ between the calibration with the quantum Hall Kelvin bridge and that with the CCC. This is compatible with zero, showing the agreement between the two calibrations of the NIST SP036 resistance standard. The uncertainty is dominated by the type A component of the bridge reading.

Figure 13 reports the results of four comparisons.

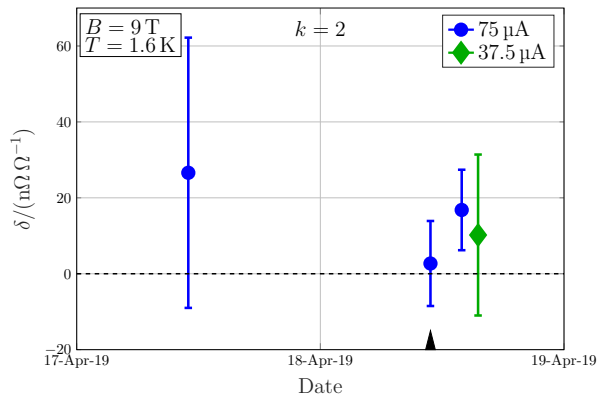

Figure 13. Summary plot of the final results of δ of four comparisons as represented in figure 11. δ, as given in (21), represents the difference between the calibration with the quantum Hall Kelvin bridge and that with the CCC. The uncertainty bars represent the expanded uncertainties with coverage factor $k = 2$.

The uncertainty bars represent the expanded uncertainties with coverage factor $k = 2$. The uncertainty budget of table 1 refers to the measurement identified in the figure with a black triangle. One of the reported measurements was obtained with a current $I_x = 37.5\,\mu\text{A}$. The different uncertainties among the measurements depend on the different measurement times and, therefore, on the different type A uncertainties. Overall, figure 13 shows a good agreement between the calibrations performed with the quantum Hall Kelvin bridge and the CCC. The single non-compatible measurement and the fact that all the deviations are positive may be likely ascribed to the characterization of the imperfect quantization of the Hall bars, in particular that of U_2. In fact, as described in section 3, U_2 was characterized through an arrangement which differs from that of operation.

Taking into account the uncertainty components

from 2 to 7 in table 1, that is, assuming perfect device quantization, the evaluation of the uncertainty here presented shows that the quantum Hall Kelvin bridge can reach an uncertainty level of a few parts in 10^9. This uncertainty level is comparable to that of a CCC calibration, in both cases mainly limited by the type A uncertainty. For the quantum Hall Kelvin bridge, taking into account the limitations described in the foregoing analysis of component 1, the type A uncertainty can be probably reduced with a more compact implementation.

8. Further developments

The quantum Hall Kelvin bridge-on-a-chip can be extended to calibrate resistance standards with nominal values different from R_H by employing in one or more arms a quantum Hall array resistance standard (QHARS). For instance, this would allow the direct calibration of resistance standards with decadal values.

It is worth noting that the usage of a QHARS for each bridge arm may reduce the number of the required QHE elements with respect to a resistance comparison with a single QHARS. In fact, for instance, let us consider $R_x \approx 1\,\mathrm{M\Omega}$, a resistance value that can be obtained, with good approximation, as $(10150/131)R_\mathrm{H}$ with a QHARS with 88 QHE elements [20, 32]. From figure 2, the bridge balance equation would yield

$$R_x \approx \frac{10150}{131} R_\mathrm{H} = \frac{R_1 R_3}{R_2}, \tag{23}$$

which can be decomposed as

$$\frac{10150}{131} R_\mathrm{H} = \frac{10 R_\mathrm{H} \times 5 R_\mathrm{H}}{\frac{131}{203} R_\mathrm{H}} = \frac{R_1 R_3}{R_2}. \tag{24}$$

This means that the $1\,\mathrm{M\Omega}$ resistance standard can be calibrated with a quantum Hall Kelvin bridge with $R_1 = 10R_\mathrm{H}$ (10 QHE elements), $R_2 = (131/203)R_\mathrm{H}$ (12) and $R_3 = 5R_\mathrm{H}$ (5). This bridge can then be implemented with just 27 QHE elements.

More generally, a resistance

$$R_x \approx \frac{p}{q} R_\mathrm{H} = \frac{p_1 p_2 p_3}{q_1 q_2 q_3} R_\mathrm{H} = \frac{R_1 R_3}{R_2}, \tag{25}$$

where p_1, p_2, p_3, q_1, q_2 and q_3 are suitable integer factors of the integers p and q, can be calibrated with a bridge with $R_1 = (p_1/q_1)R_\mathrm{H}$, $R_2 = (q_2/p_2)R_\mathrm{H}$ and $R_3 = (p_3/q_3)R_\mathrm{H}$. This arrangement might need fewer QHE elements than those of a QHARS with resistance $(p/q)R_\mathrm{H}$. In this configuration, the effect of the lead resistances can be minimized by adjusting the combining network composed of r_1 and r_4.

9. Conclusions

The quantum Hall Kelvin bridge presented in this work has shown an accuracy at the level of a few parts in 10^8 when calibrating an artefact standard resistor with nominal value R_H, at present mainly limited by the prototype device and the interferences in the current implementation, with the potential to achieve few parts in 10^9. This result is comparable with that of other state-of-the-art calibration bridges, like the DCC or the CCC. The bridge includes just two room temperature electronic instruments of standard accuracy. The implementation as graphene bridge-on-a-chip is particularly simple and robust and allows the connection to the room temperature standard resistor and electronics with few leads.

With respect to a CCC with a QHR, the quantum Hall Kelvin bridge can be implemented with a single cryogenic environment, suitable for operation in a dry cryocooler. Furthermore, this can be of small size when graphene is adopted for the QHE elements. At variance with DCC or CCC instruments, the noise rejection (which depends on a voltmeter) is expected to be significantly higher.

The usage of QHARS can extend the operation of the quantum Hall Kelvin bridge to resistance standards of arbitrary nominal value.

Acknowledgments

Martina Marzano thanks Randolph E. Elmquist and the Fundamental Electrical Measurements Group for supporting her stay at NIST, Gaithersburg, MD, US, and this work. The work of Dinesh K. Patel at NIST was made possible by C-T Liang of National Taiwan University. The authors thank C-I Liu and A Levy for their assistance with the NIST internal review process.

References

[1] J. Williams, "Cryogenic current comparators and their application to electrical metrology," *IET Science, Measurement & Technology*, vol. 5, pp. 211–224, Nov. 2011.

[2] A. R. Panna, M. E. Kraft, A. F. Rigosi, G. R. Jones, S. U. Payagala, M. Kruskopf, D. G. Jarrett, and R. E. Elmquist, "Uncertainty of the ohm using cryogenic and non-cryogenic bridges," in *2018 Conference on Precision Electromagnetic Measurements (CPEM 2018)*, Paris, France, Jul. 2018, pp. 1–2.

[3] M. Marzano, L. Callegaro, and M. Ortolano, "A quantum Hall effect Kelvin bridge for resistance calibration," in *2018 Conference on Precision Electromagnetic Measurements (CPEM 2018)*, Paris, Jul. 2018.

[4] M. Kruskopf, A. F. Rigosi, A. R. Panna, D. K. Patel, H. Jin, M. Marzano, M. Berilla, D. B. Newell, and R. E. Elmquist, "Two-terminal and multi-terminal designs for next-generation quantized Hall resistance standards: contact material and geometry," *IEEE Trans. Electron Devices*, vol. 66, no. 9, pp. 3973–3977, 2019.

[5] M. Kruskopf, A. F. Rigosi, A. R. Panna, M. Marzano, D. Patel, H. Jin, D. B. Newell, and R. E. Elmquist, "Next-generation crossover-free quantum Hall arrays with superconducting interconnections," *Metrologia*, vol. 56, no. 6, p. 065002, Oct. 2019.

[6] R. Ribeiro-Palau, F. Lafont, J. Brun-Picard, D. Kazazis, A. Michon, F. Cheynis, O. Couturaud, C. Consejo, B. Jouault, W. Poirier, and F. Schopfer, "Quantum Hall resistance standard in graphene devices under relaxed experimental conditions," *Nature Nanotech.*, vol. 10, pp. 965–971, 2015.

[7] M. Kruskopf and R. E. Elmquist, "Epitaxial graphene for quantum resistance metrology," *Metrologia*, vol. 55, pp. R27–R36, Jul 2018.

[8] A. F. Rigosi and R. E. Elmquist, "The quantum Hall effect in the era of the new SI," *Semicond. Sci. Technol.*, vol. 34, no. 9, p. 093004, aug 2019.

[9] T. J. B. M. Janssen, S. Rozhko, I. Antonov, A. Tzalenchuk, J. M. Williams, Z. Melhem, H. He, S. Lara-Avila, S. Kubatkin, and R. Yakimova, "Operation of graphene quantum Hall resistance standard in a cryogen-free table-top system," *2D Materials*, vol. 2, no. 3, p. 035015, aug 2015.

[10] A. F. Rigosi, A. R. Panna, S. U. Payagala, M. Kruskopf, M. E. Kraft, G. R. Jones, B.-Y. Wu, H.-Y. Lee, Y. Yang, J. Hu, D. G. Jarrett, D. B. Newell, and R. E. Elmquist, "Graphene devices for tabletop and high-current quantized Hall resistance standards," *IEEE Trans. Instrum. Meas.*, vol. 68, no. 6, pp. 1870–1878, Dec. 2019.

[11] F. Delahaye, "Series and parallel connection of multiterminal quantum Hall effect devices," *J. Appl. Phys.*, vol. 73, pp. 7914–7920, 1993.

[12] F. Schopfer and W. Poirier, "Testing universality of the quantum Hall effect by means of the Wheatstone bridge," *J. Appl. Phys.*, vol. 102, p. 054903, 2007.

[13] ——, "Quantum resistance standard accuracy close to the zero-dissipation state," *J. Appl. Phys.*, vol. 114, p. 064508, 2013.

[14] B. W. Ricketts and P. C. Kemeny, "Quantum Hall effect devices as circuit elements," *J. Phys. D: Appl. Phys.*, vol. 21, p. 483, 1988.

[15] L. Callegaro, *Electrical impedance: principles, measurement, and applications*, ser. in Sensors. Boca Raton, FL, USA: CRC press: Taylor & Francis, 2013, iSBN: 978-1-43-984910-1.

[16] Bureau International des Poids et Mesures, "9th SI brochure," 2019. [Online]. Available: www.bipm.org

[17] S. W. Chua, B. P. Kibble, and A. Hartland, "Comparison of capacitance with AC quantized Hall resistance," *IEEE Trans. Instrum. Meas.*, vol. 48, pp. 342–345, 1999. [Online]. Available: http://ieeexplore.ieee.org/document/769597/

[18] L. Callegaro, V. D'Elia, and B. Trinchera, "Realization of the farad from the dc quantum Hall effect with digitally assisted impedance bridges," *Metrologia*, vol. 47, pp. 464–472, 2010.

[19] F. P. M. Piquemal, J. Blanchet, G. Gèneves, and J.-P. André, "A first attempt to realize (multiple-QHE devices)-series array resistance standards," *IEEE Trans. Instrum. Meas.*, vol. 48, no. 2, pp. 296–300, 1999.

[20] M. Ortolano, M. Abrate, and L. Callegaro, "On the synthesis of quantum Hall array resistance standards," *Metrologia*, vol. 52, pp. 31–39, 2015.

[21] V. Panchal, Y. Yang, G. Cheng, J. Hu, M. Kruskopf, C.-I. Liu, A. F. Rigosi, C. Melios, A. R. H. Walker, D. B. Newell, O. Kazakova, and R. E. Elmquist, "Confocal laser scanning microscopy for rapid optical characterization of graphene," *Communications Physics*, vol. 1, no. 1, nov 2018.

[22] M. Kruskopf, D. M. Pakdehi, K. Pierz, S. Wundrack, R. Stosch, T. Dziomba, M. Götz, J. Baringhaus, J. Aprojanz, C. Tegenkamp, J. Lidzba, T. Seyller, F. Hohls, F. J. Ahlers, and H. W. Schumacher, "Comeback of epitaxial graphene for electronics: large-area growth of bilayer-free graphene on SiC," *2D Materials*, vol. 3, no. 4, p. 041002, sep 2016.

[23] Y. Yang, G. Cheng, P. Mende, I. G. Calizo, R. M. Feenstra, C. Chuang, C.-W. Liu, C.-I. Liu, G. R. Jones, A. R. H. Walker, and R. E. Elmquist, "Epitaxial graphene homogeneity and quantum Hall effect in millimeter-scale devices," *Carbon*, vol. 115, pp. 229–236, may 2017.

[24] A. F. Rigosi, M. Kruskopf, H. M. Hill, H. Jin, B.-Y. Wu, P. E. Johnson, S. Zhang, M. Berilla, A. R. H. Walker, C. A. Hacker, D. B. Newell, and R. E. Elmquist, "Gateless and reversible carrier density tunability in epitaxial graphene devices functionalized with chromium tricarbonyl," *Carbon*, vol. 142, pp. 468–474, feb 2019.

[25] M. Götz and D. Drung, "Stability and performance of the binary compensation unit for cryogenic current comparator bridges," *IEEE Trans. Instrum. Meas.*, vol. 66, no. 6, pp. 1467–1474, jun 2017.

[26] M. Ortolano and L. Callegaro, "Matrix method analysis of quantum Hall effect device connections," *Metrologia*, vol. 49, no. 1, p. 1, 2012.

[27] M. Marzano, T. Oe, M. Ortolano, L. Callegaro, and N. H. Kaneko, "Error modelling of quantum Hall array resistance standards," *Metrologia*, vol. 55, pp. 167–174, 2018.

[28] C. M. Sutton and M. T. Clarkson, "A general approach to comparisons in the presence of drift," *Metrologia*, vol. 30, pp. 487–493, 1994.

[29] H. E. Swanson and S. Schlamminger, "Removal of zero-point drift from AB data and the statistical cost," *Meas. Sci. Technol.*, vol. 21, p. 115104, 2010.

[30] S. A. Awan, B. Kibble, and J. Schurr, *Coaxial Electrical Circuits for Interference-Free Measurements*, ser. IET electrical measurement series. Institution of Engineering and Technology, 2011, ch. 6, pp. 173–176.

[31] J. A. Barnes, A. R. Chi, L. S. Cutler, D. J. Healey, D. B. Leeson, T. E. McGunigal, J. A. Mullen, W. L. Smith, R. L. Sydnor, R. F. C. Vessot, and G. M. R. Winkler, "Characterization of frequency stability," *IEEE Trans. Instrum. Meas.*, vol. IM-20, pp. 105–120, 1971.

[32] T. Oe, S. Gorwadkar, T. Itatani, and N. H. Kaneko, "Development of 1 MΩ quantum Hall array resistance standards," *IEEE Trans. Instrum. Meas.*, vol. 66, no. 6, pp. 1475–1481, June 2017.